POLITECNICO DI TORINO
Repository ISTITUZIONALE

Efficient broadband sound absorption exploiting rainbow labyrinthine metamaterials

Original
Efficient broadband sound absorption exploiting rainbow labyrinthine metamaterials / Nistri, F., Kamrul, V.H., Bettini, L., Musso, E., Piciucco, D., Zemello, M., Gliozzi, A.S., Krushynska, A.O., Pugno, N., Sangiuliano, L., Shtrepi, L., Bosia, F.. - In: JOURNAL OF PHYSICS D. APPLIED PHYSICS. - ISSN 0022-3727. - 57:24(2024). [10.1088/1361-6463/ad3012]

Availability:
This version is available at: 11583/2989446 since: 2024-06-11T21:11:06Z

Publisher:
IOP Publishing

Published
DOI:10.1088/1361-6463/ad3012

Terms of use:

This article is made available under terms and conditions as specified in the corresponding bibliographic description in the repository

Publisher copyright

(Article begins on next page)

19 November 2026

Journal of Physics D: Applied Physics

PAPER • OPEN ACCESS

Efficient broadband sound absorption exploiting rainbow labyrinthine metamaterials

To cite this article: F Nistri *et al* 2024 *J. Phys. D: Appl. Phys.* **57** 245111

View the article online for updates and enhancements.

You may also like

- Beam aperture modifier design with acoustic metasurfaces
Weipeng Tang and Chunyu Ren
- Broadband diffuse reflections of sound by metasurface with random phase response
Zhong-ming Gu, Bin Liang, Xin-ye Zou et al.
- Spider web-structured labyrinthine acoustic metamaterials for low-frequency sound control
A O Krushynska, F Bosia, M Miniaci et al.



This content was downloaded from IP address 130.192.232.210 on 21/03/2024 at 12:36

OPEN ACCESS
IOP Publishing
Journal of Physics D: Applied Physics
J. Phys. D: Appl. Phys. **57** (2024) 245111 (12pp)
https://doi.org/10.1088/1361-6463/ad3012

Efficient broadband sound absorption exploiting rainbow labyrinthine metamaterials

F Nistri[1], V H Kamrul[2], L Bettini[2], E Musso[2], D Piciucco[2], M Zemello[2], A S Gliozzi[1], A O Krushynska[3], N Pugno[4,5], L Sangiuliano[6], L Shtrepi[7] and F Bosia[1,*]

[1] Department of Applied Science and Technology, Politecnico di Torino, Torino, Italy
[2] Politecnico di Milano, Milano, Italy
[3] Faculty of Science and Engineering, University of Groningen, Groningen, The Netherlands
[4] Laboratory for Bioinspired, Bionic, Nano, Meta Materials & Mechanic, University of Trento, Trento, Italy
[5] School of Engineering and Materials Science, Queen Mary University of London, London, United Kingdom
[6] Phononic Vibes s.r.l., Milano, Italy
[7] Department of Energy 'Galileo Ferraris', Politecnico di Torino, Torino, Italy

E-mail: federico.bosia@polito.it

Received 7 December 2023, revised 19 January 2024
Accepted for publication 4 March 2024
Published 21 March 2024

Abstract

In this work, we demonstrate in a proof of concept experiment the efficient noise absorption of a 3D printed panel designed with appropriately arranged space-coiling labyrinthine acoustic elementary cells of various sizes. The labyrinthine unit cells are analytically and numerically analysed to determine their absorption characteristics and then fabricated and experimentally tested in an impedance tube to verify the dependence of absorption characteristics on cell thickness and lateral size. The resonance frequency of the unit cell is seen to scale approximately linearly with respect to both thickness and lateral size in the considered range, enabling easy tunability of the working frequency. Using these data, a flat panel is designed and fabricated by arranging cells of different dimensions in a quasi-periodic lattice, exploiting the acoustic 'rainbow' effect, i.e. superimposing the frequency response of the different cells to generate a wider absorption spectrum, covering the target frequency range, chosen between 800 and 1400 Hz. The panel is thinner and more lightweight compared to traditional sound absorbing solutions and designed in modular form, so as to be applicable to different geometries. The performance of the panel is experimentally validated in a small-scale reverberation room, and an absorption close to ideal values is demonstrated at the desired frequencies of operation. Thus, this work suggests a design procedure for noise-mitigation panel solutions and provides experimental proof of the versatility and effectiveness of labyrinthine metamaterials for tunable mid- to low-frequency sound attenuation.

Keywords: wave dynamics, acoustic metamaterials, noise control

* Author to whom any correspondence should be addressed.

Original content from this work may be used under the terms of the Creative Commons Attribution 4.0 licence. Any further distribution of this work must maintain attribution to the author(s) and the title of the work, journal citation and DOI.

© 2024 The Author(s). Published by IOP Publishing Ltd

1. Introduction

In recent years, acoustic metamaterials (AMs) have gained widespread attention because of their exceptional properties, which are not commonly found in naturally occurring materials [1–3]. AMs could potentially pave the way to the development of a new generation of acoustic absorbers and diffusers with deep-subwavelength thickness, that can be tailored for a desired frequency spectrum [4]. Their use brings new possibilities to the traditional problem of achieving low-frequency absorption [5]. In addition, AMs offer the possibility to achieve high performance in terms of noise reduction, and simultaneously reduced size and weight of structures [6], going beyond the limitations of conventional technologies based on single layer mass law, double layer resonance frequency tuning and porous absorber thickness optimization [7]. In particular, these new materials seem to be promising and to respond to the thickness and weight constraints imposed by the design/technological requirements of the market, e.g. in aircraft cabin design in aeronautics [8]. AMs can be combined with conventional solutions like porous materials [9, 10], Helmholtz resonators [11] or tensioned membranes [12, 13] for tuned or optimized performance. It is well known that perfect absorption can be obtained when a critical coupling condition occurs, whereby thermo-viscous losses are exactly balanced by the energy leakage [14]. Such perfect absorption in a subwavelength regime has for example been shown to be achievable with periodic arrays of vertical Helmholtz resonators [15], as well as with plate-resonator/closed waveguide structures [16]. However, the working frequencies of these AMs are often quite narrow, or the structures need to be bulky to enable broadband operation. To address this problem, the concept of 'rainbow trapping' in acoustic resonators with variable parameters, and hence working frequencies [17–20] or systems with asymmetric porous absorbers [21] has been adopted so far.

A particularly interesting type of AM that has emerged in recent years are 'labyrinthine' or 'coiled' structures [22]. These are based on exploiting acoustic wave propagation in curved channels of subwavelength cross-section, giving rise to an extremely high effective refractive index (and thus to a decrease of the effective wave speed) and the possibility of achieving 'double negativity', i.e. simultaneously negative effective density and bulk modulus, or conical dispersion [23, 24]. Tapered two-dimensional (2D) labyrinthine designs have also been shown to achieve optimal broadband impedance matching, which is fundamental for efficient absorption [25]. The concept has also been extended from 2D to 3D space coiling labyrinthine structures [26]. Experimental demonstrations of the theoretically predicted broadband negative refractive index have been achieved through reflection or transmission measurements and two-dimensional prism-based measurements on 3D printed thermoplastic labyrinthine samples [23]. Hilbert-like fractal AMs have also been designed, fabricated via 3D printing, and experimentally characterized, to achieve efficient low-frequency acoustic wave attenuation [27, 28]. 3D 'one-port' labyrinthine structures have also been proposed to achieve high-levels of sound absorption over large frequency ranges (and for various incidence angles), exploiting different channel lengths to tune the operating bands [29]. Another example of labyrinthine AM providing large tunability are spider-web inspired structures, in which the addition of edge cavities can further enhance the possibilities to manipulate dispersion properties, control the appearance of band gaps or negative group velocity, and tailor transmission/reflection characteristics [30]. Several studies have shown that the use of space filling structures, such as Wunderlich curves, can efficiently control transmission, reflection and absorption by varying channel tortuosity, so that total broadband reflection/absorption can be achieved e.g. by tuning the channel length [31, 32].

Thus, labyrinthine and space-filling AMs have provided a very convenient and efficient way to achieve sound control in large frequency ranges, especially in the subwavelength regime, by tuning geometrical design parameters (e.g. channel tortuosity or elongation and cavity size). This kind of adaptability could largely benefit noise absorption applications at small to medium scale, where restrictions on structural size of the absorbers impose trade-offs between efficiency and encumbrance. Sufficiently thick conventional acoustic absorbing materials, such as glass wool or foams within sandwich panels with an average density of 50–75 kg m^{-3} [33] can absorb acoustic wave energy in wide frequency ranges, but their bulky characteristics limit their broad application for low frequency absorption. Moreover, lightweight characteristics become crucial when dealing with devices in the aerospace and automotive industry or other technological domains [8]. At present, few studies [34] in the literature have presented detailed acoustic characterization studies on large structures such as metamaterial-based panels, and none on labyrinthine ones, to the best of our knowledge. Further, the need emerges to investigate labyrinthine AM performance on structures that are closer to potential operating conditions, i.e. in diffuse field conditions.

With this in mind, the present study investigates the design of coiled labyrinthine acoustic resonators, their appropriate combination in a 3D printed 'rainbow' panel and presents a proof-of-concept experiment to demonstrate efficient broadband noise absorption. The paper describes the following workflow. Design of labyrinthine unit cells (UCs) and analytical model of their absorption spectra is described in section 2. Experimental and numerical characterization and comparison with the analytical model for the designed UC is provided in section 3. Design and 3D printing of a full-scale panel with variable, appropriately chosen constituent UC dimensions, its numerical model and experimental test in a reverberation room is described in section 4. Finally, a numerical investigation of a coupling of the panel with conventional absorbing material is described in section 5.

2. Unit cell design and analysis

In conventional ideal fluid environments, sound propagation is typically described by a lossless wave equation [35–37]. However, when fluids are confined in small regions, like

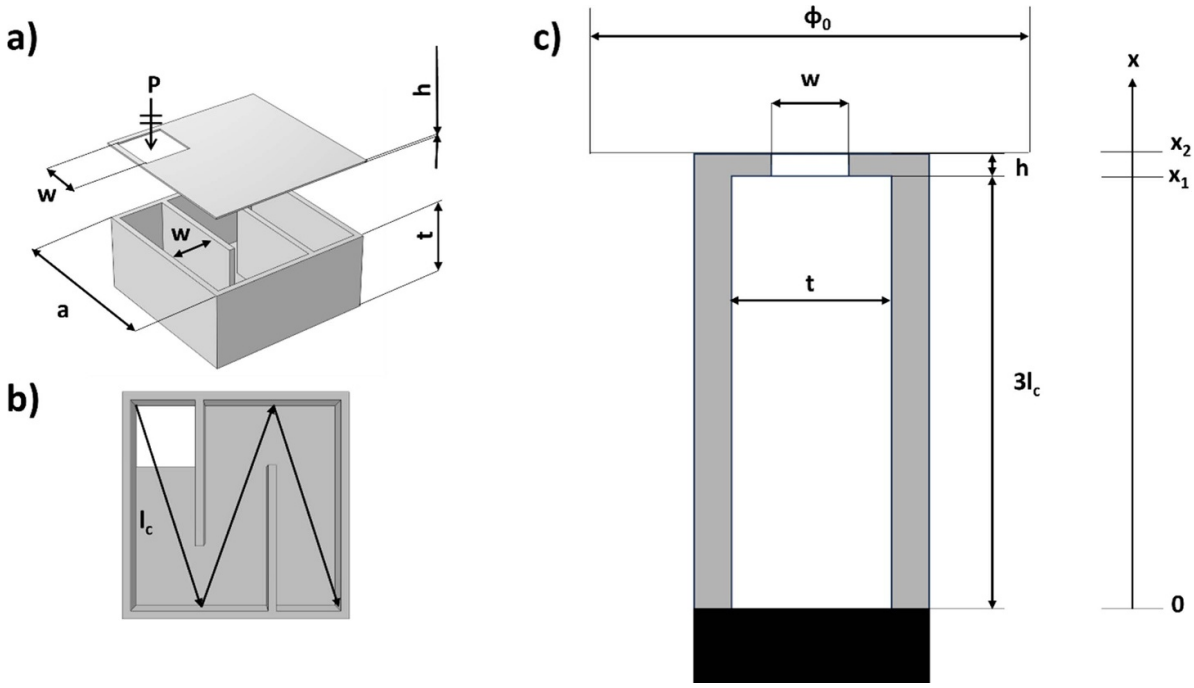


Figure 1. (a) 1st iteration Wunderlich curve UC with $w = 6$ mm, $t = 9.6$ mm, $a = 19.6$ mm and $h = 0.5$ mm. (b) Schematic of the effective distance travelled by the pressure wave inside the cavity. (c) Schematic of the equivalent model with the tube of variable cross section closed by a reflecting backing and open on one side.

narrow tubes or slits, it is necessary to account for structural losses [30, 33]. There are two primary loss mechanisms: thermal losses, mainly arising from heat diffusion at the boundaries within the sound field, and viscous losses, due to friction with the UC walls. These physical dissipation mechanisms effectively absorb sound energy, leading to perfect absorption when they are balanced by the acoustic energy leakage by radiation from the UC: the matching of the two corresponds to the critical coupling condition [14, 36].

The type of labyrinthine geometry considered in this work (figure 1(a)) is a first-iteration Wunderlich curve [38], which corresponds to a quarter-wave resonator. This design can be studied using narrow tube thermo-viscous loss models to derive its absorption properties. In particular, the designed aperture (figure 1(a)) is responsible both for the losses and energy leakage of the UC, while the cavity (figure 1(b)) is only responsible for the losses. The considered UC can be modeled as a tube with constant cross section $w \times t$, and a rigid backing (figure 1(c)) as pointed out by several works [39–41]. In particular, given the subwavelength size of the system, the equivalent tube can be described as a narrow duct, following Stinson's approximation for thermo-viscous losses [42], while the inlet can be studied as a perforated plate using the Johnson-Champoux-Allard (JCA) model, as described in [39].

Thus, calculating the impedance of the equivalent model at the surface (Z_s), the acoustic absorption (α) can be computed as:

$$\alpha = 1 - \left| \frac{Z_s - Z_0}{Z_s + Z_0} \right|^2, \tag{1}$$

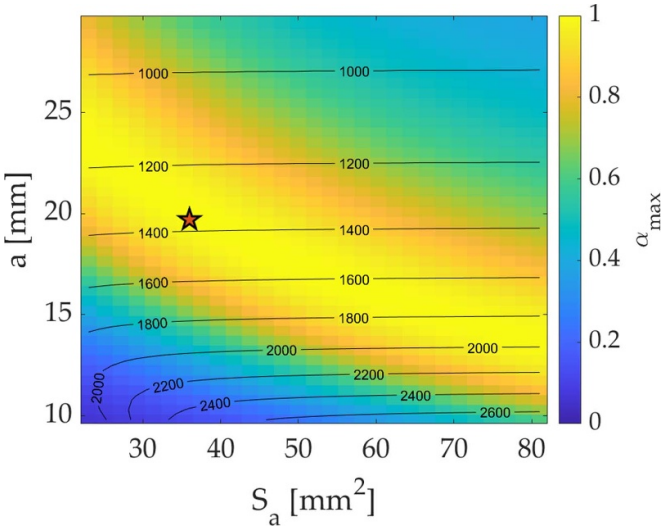


Figure 2. Maximum absorption map vs the edge size a vs the aperture cross section S_a of the UC. The contour lines represent the frequencies of maximum absorption, and the star is the selected UC size.

where $Z_0 = \rho_0 c_0$, $\rho_0 = 1.225\ \mathrm{kg\,m^{-3}}$ are the impedance and air density respectively and $c_0 = 343\ \mathrm{m\ s^{-1}}$ is the speed of sound in air [29]. The value Z_s and its derivation are provided in appendix.

A parametric study of the analytical model is carried out (figure 2) to study the dependence of maximum sound absorption $\alpha_{\max}$ on the edge size a (scaling the UC isotropically in the plane), ranging from 10–29 mm, and the aperture cross section S_a from approximately 22–80 mm^2. The thickness $t = 9.6$ mm

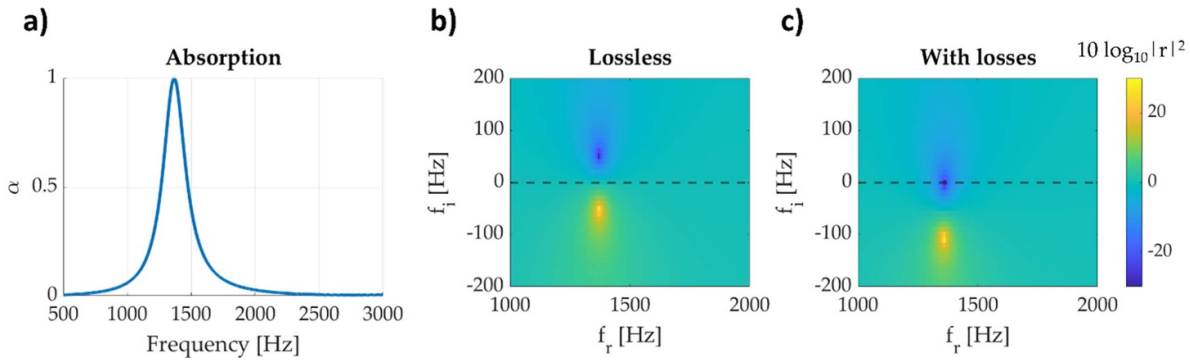


Figure 3. (a) absorption spectrum for the 1st iteration Wunderlich curve UC. Reflectance of the UC represented on the complex frequency plane for (b) the 'lossless' and (c) 'lossy' case, where thermo-viscous dissipation occurring at the boundary between the air and the cell walls is neglected/accounted for, respectively.

is fixed to obtain a subwavelength thickness in the investigated frequency ranges. From the four-parameter map obtained, a UC featuring perfect absorption in the targeted frequency range ($a = 19.7$ mm and $S_a = 36$ mm^2) is selected. The cross section S_a is chosen so as to allow measurements in an impedance tube (see section 3).

The analytically calculated absorption spectra of the UC (figure 3(a)) confirm that perfect absorption is attained at 1370 Hz with a peak width of $\Delta f = 110$ Hz. In addition, to gain further insight on the absorption phenomenon, the reflectance $|r|^2 = 1 - \alpha$ of the UC is represented in the complex frequency plane using the method introduced by Romero-Garcia *et al* [14]. As shown in figure 3(b) in the lossless case, the reflectance shows a zero/pole complex conjugate pair attained at the resonance frequency of the UC. When losses are introduced in the model, the pair is shifted towards smaller imaginary frequencies and the critical coupling condition [14] is obtained when the losses balance the energy leakage. In this case, the zero falls exactly on the real frequency axis, resulting in perfect absorption (figure 3(c)).

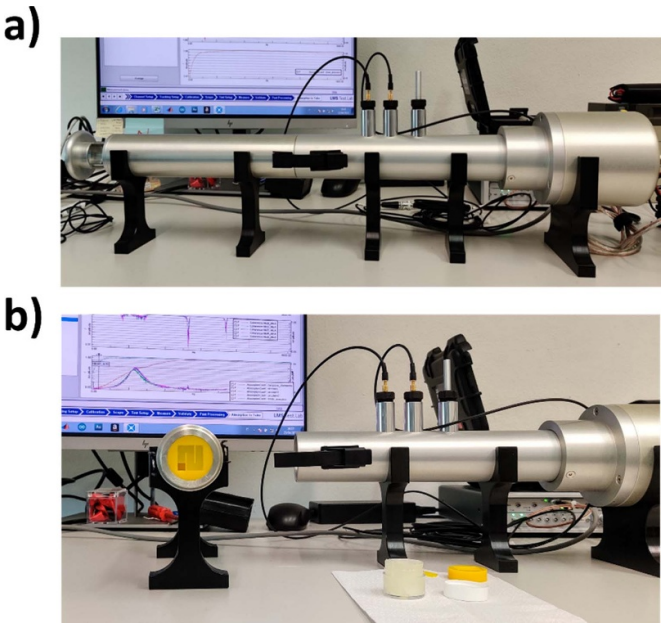


Figure 4. Experimental setup for impedance tube measurements. (a) The complete impedance tube setup. (b) Open tube with sample mounted in its holder.

3. UC experimental and numerical characterization

In order to validate the design predictions and experimentally assess the efficiency of the UC subwavelength sound wave absorption, we first perform normal incidence measurements on various types of UCs in an impedance tube. The UCs consist of a square cavity inside a solid cylinder, in which internal solid walls form a labyrinthine pattern. The UC samples for impedance tube measurements are manufactured in PLA using a Dremel Digilab filament 3D printer and in VeroYellow using a Stratasys J750 FDM 3D printer. The two polymers have similar mechanical characteristics, which are compatible with the rigid wall hypothesis used in simulations.

The impedance tube setup is depicted in figure 4. The impedance measurements are performed in accordance with ISO 10534-2 [43] and ASTM E1050-19 [44] (two-microphone technique) regulations, in order to measure the normal incidence absorption coefficient (α_0), calculated for a normally impinging pressure wave [45]. Measurements are performed using a HW-ACT-TUBE and -STL (Siemens, Munich, Germany), which has an inner diameter of 35 mm with relative cut-off frequency $f_c \sim 5600$ Hz [46] and is equipped with two ¼' flush mounted GRAS 46BD microphones (GRAS, Holte, Denmark) and a white noise source, i.e. a 2' aluminium driver. The method allows to obtain accurate sound pressure amplitude and phase measurements in the whole frequency range of interest, i.e. 100–5000 Hz [45], with a spectral resolution of 2 Hz. The sample holder consists of a tube with a sliding rigid piston. A specific plastic sample holder is used as shown in figure 4(b). The method allows a better control on the positioning of the different samples into the flanged sample holder of the tube. The 3D printed samples have a reflective overall surface and a diameter allowing for

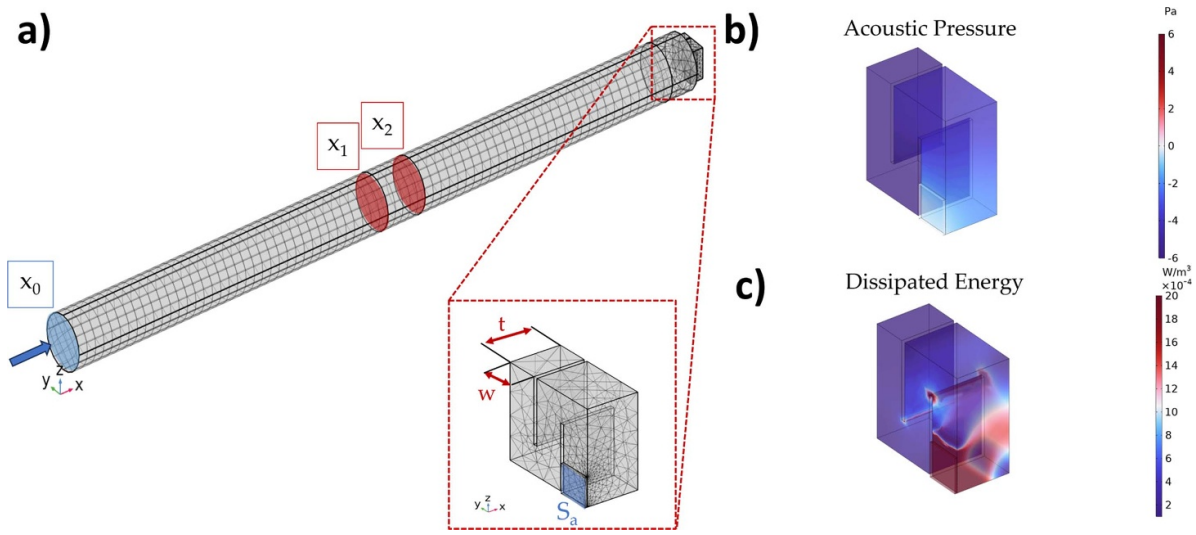


Figure 5. (a) FE mesh in the model of the impedance tube containing the labyrinthine UC. Blue transparency region corresponds to the area of application of the boundary pressure, while the red ones to the areas where the average pressure is sampled. In the inset, the blue transparency region highlights the domain where the poroacustic conditions (JCA in analytical model) are applied and the cross-section sizes of the UC used for the narrow region change. (b) Acoustic pressure field and (c) dissipated energy inside the UC at the peak absorption frequency, with corresponding colour scale.

tolerances such that the circumferential effect discussed in [47] can be considered negligible. The effect of any possible irregularity in the samples, and in particular at the edges, is taken into consideration by repeating the tests for each structure with three nominally identical samples, to evaluate reproducibility. Temperature and atmospheric pressure are monitored by calibrated transducers. The acoustic pressure is measured by two microphones set at a distance of 29 mm from each other along the length of the tube. The absorption coefficient spectrum $\alpha(f)$ of the UC is obtained using the transfer function method [35]. This procedure is repeated several times for each experimental configuration to reduce dispersion in the measurements.

For further comparison, a numerical finite element (FE) model reproducing the experimental setup is implemented, as shown in figure 5(a), comprising the air domains of the tube, the aperture, and the UC. The model is implemented in COMSOL Multiphysics and is performed using the Acoustics module and 'narrow region' condition for the tube and the UC, and 'poro-acoustic' one for the aperture. At the boundary located at the position x_0, a plane wave radiation of the form $P = Ae^{ik_0x}$ is applied, with $A = 1$ Pa, $k_0 = 2\pi f/c_0$, while the average pressure at the cross section of the tube is sampled at the surfaces located at x_1 and x_2 to compute the transfer function, and the absorption. Figure 5(b) shows the pressure field at the peak absorption frequency, where we observe a spatial distribution that increases up to six times the input pressure amplitude, in absolute value, while remaining equal at the aperture. Due to this gradient in pressure, the particle velocity increases accordingly. Figure 5(c) shows the dissipated energy which is concentrated in the aperture region, with a smaller contribution from the cavity, due to the larger friction in the latter.

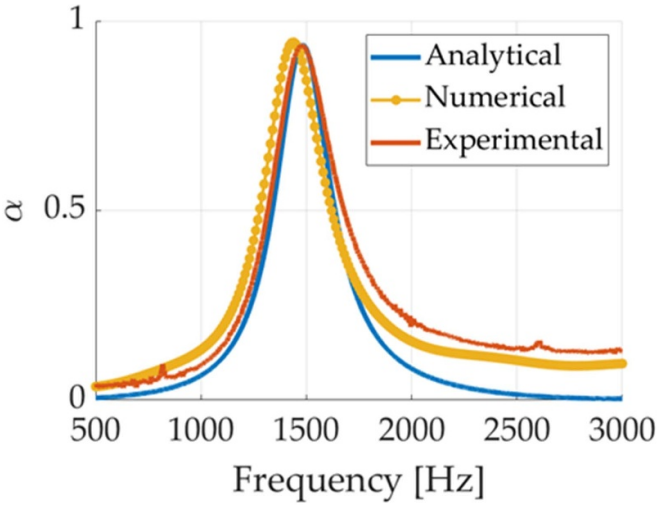


Figure 6. Comparison of analytical, numerical and experimental absorption spectra.

A comparison of the analytical, numerical, and experimental absorption spectra of one of the labyrinthine UCs is shown in figure 6, as an illustrative example. The tested sample has a UC lateral size of $a = 19.7$ mm and a thickness of $t = 9.6$ mm. The experimental absorption spectrum features an absorption coefficient of $\alpha = 0.95$, at a frequency $f_{\text{exp}} \sim 1480$ Hz with a peak width of $\Delta f_{\text{exp}} \sim 390$ Hz. This result is used to calibrate the analytical model's correction factors $\psi = 8.4 \times 10^{-2} L$ and $\alpha_s = 1.9$ (see appendix). Although excellent matching is achieved in the neighborhood of the absorption peak frequency, the analytical curve underestimates the absorption for the other frequency ranges and the

width of the peak by ca. 70 Hz. This underestimation is probably due to the missing thermo-viscous losses taking place on the walls of the tube itself, which are instead present in the FE simulation. In the numerical model, although the peak frequency is underestimated by 40 Hz, the spectrum presents a larger absorption for lower and higher frequencies with respect to the peak and accurately predicts the peak bandwidth $\Delta f_{\text{num}} \sim 360$ Hz obtained in experimental results, together with the correct behavior in the higher frequency range.

Given the objective designing a rainbow panel, the resonance frequency dependence on the dimensions of the UC cavity is studied [21]. In order to quantify the resonance frequency dependence on the geometrical size, several UCs similar to the ones in figure 1 were manufactured, varying both in thickness t (within the 10.0–25.0 mm range, keeping their UC edge size a fixed to 21.2 mm) and lateral edge size a (within the 13.0–20.0 mm range, keeping their thickness t fixed to 12.6 mm). Analytical, numerical and experimental results in figures 6(a) and (b) show the frequency peak value vs thickness t and edge size a, respectively. The analytical model underestimates the peak frequencies somewhat, due to the fact that the empirical correction factors α_s and ψ (see appendix) are maintained constant for the different sizes, without performing any fitting of the model. Despite this, there is a fairly good agreement with numerical and experimental results. The resonance frequency scales approximately linearly by a factor $\frac{\mathrm{d}f_r}{\mathrm{d}t} = -42.7$ Hz mm^{-1} with the sample thickness t, and by a factor $\frac{\mathrm{d}f_r}{\mathrm{d}a} = -145.3$ Hz mm^{-1} with the UC edge size a. Thus, the influence of the UC lateral edge size allows to tune the working frequency in a larger interval, while the thickness dependency can be employed to fine-tune the frequency in a smaller frequency range to the desired value.

4. Rainbow AM labyrinthine panel

4.1. Panel design and fabrication

Using impedance tube data, relative to the characterization of the chosen UC, we establish the target frequency range of interest for sound absorption (e.g. for aeronautics applications), between 800 and 1300 Hz. This can be achieved by exploiting various UCs of different lateral sizes and thicknesses, so that the resulting resonance spectrum is given by their combination, and the corresponding absorption range extends over the desired range. An AM panel is thus designed, consisting of differently sized UCs, with varying thicknesses and surface areas. The internal wall thickness of each UC is proportional to the UC edge area. Starting from two UC edge sizes ($a_1 = 19.5$ mm and $a_2 = 26.0$ mm) at different thicknesses ($t_1 = 10 \div 15$ mm for the a_1 UC, and $t_2 = 23 \div 25$ mm for the a_2 UC), a spatial pattern of repeated a_1 and a_2 UCs is conceived, covering a total module of $156 \times 156\,\text{mm}^2$ area. We define this module 'macro-cell' (M and M' in figures 7(a) and (b)) because of its intermediate size between an UC and the complete sound absorbing panel. The complete panel consists of the combination of 20 macro-cells arranged in the plane (figure 7(b)), to cover a total surface of $628 \times 784\,\text{mm}^2$, i.e. the area of the panel. Adjacent macro-cells are rotated by 90 degrees and reflected (figure 7), to ensure maximum spatial homogeneity in the sound absorbing properties.

The UCs are selected so as to provide different absorption peaks, whose superposition provides a wider working frequency spectrum in the chosen target frequency range. The arrangement of the UCs, on the other hand, is chosen so as to guarantee as far as possible spatial uniformity, whereby, at least theoretically, the overall impedance of the panel can be calculated as the combination in parallel of the impedances of the single UCs [39].

The polyamide panel is then manufactured through selective laser sintering (SLS), a technique where each level is sintered by a laser beam, directed by a scanning system. The process is repeated, and the prototype is built layer by layer. SLS is chosen as the most appropriate fabrication technique since it does not require supports to sustain oblique and horizontal protrusions and it allows to fabricate undercuts. However, to manufacture hollow structures like the UCs, it is necessary to include at least two apertures (on the top and bottom surfaces) for each UC cavity, in order to remove any residual powder from the fabrication process, so an additional opening is added for each UC. For the measurement phase, these additional openings are closed with properly sized polyamide caps that are fixed with aluminium tape to guarantee an acoustic seal. A 3D view of the final panel is shown in figure 8(c).

4.2. FE model of the AM panel

The FE model of the full panel is shown in figure 9. Periodic Bloch-Floquet boundary conditions are applied to the sides of the acoustic waveguide. A source load of plane wave radiation is applied to the wave path with the same pressure field described in the previous paragraph. The domains are modeled using approximately 540000 elements. The maximum element size is $\Delta_{\text{max}} = \frac{\lambda_{\text{min}}}{10}$, where λ_{min} is the smallest wavelength and the minimum element size is $\Delta_{\text{min}} = \frac{\lambda_{\text{min}}}{30}$. Viscous-thermal losses are modeled using the 'narrow region acoustics' model, which allows to account for the thermal and viscous losses that occur in narrow ducts where the cross-section is comparable in size to the thermal and viscous boundary layer thickness. This option allows to avoid solving a full thermo-viscous acoustic model in the whole domain. The narrow regions are defined in the front and back caps and in the UC cavities. The loss is calculated based on rectangular duct, taking the width (w) and the thickness (t) of the duct as parameters. In the configurations where the back caps are closed, no narrow regions are applied. Boundary walls are considered perfectly rigid, since results from fully vibro-acoustic (not shown) and simple acoustic simulations give rise to negligible differences.

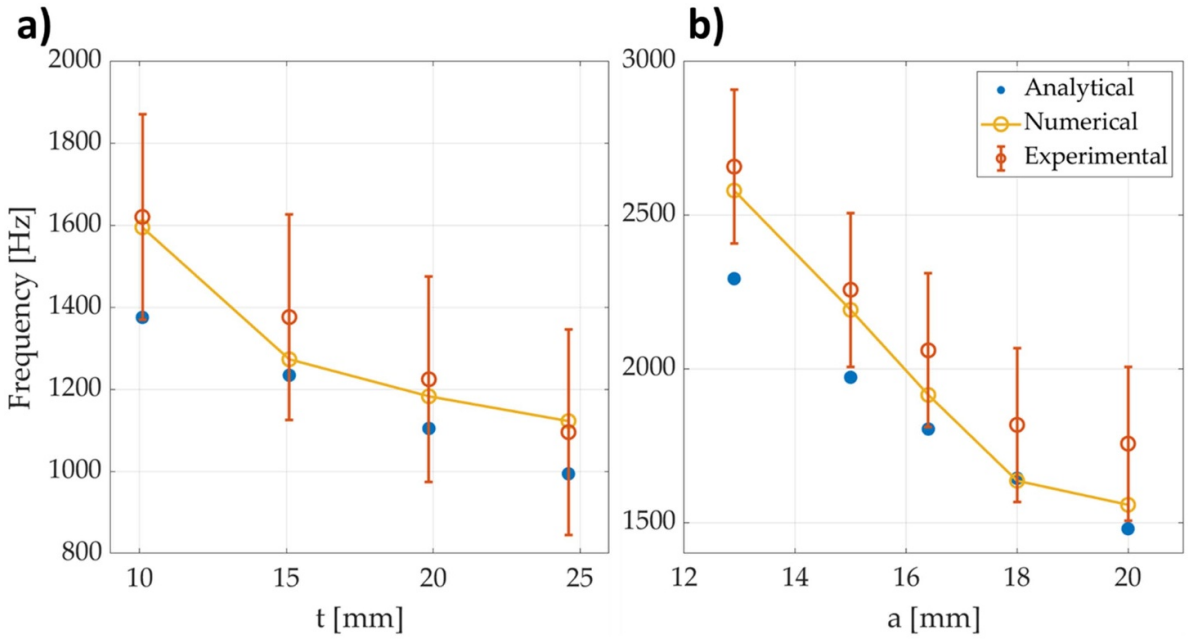


Figure 7. Absorption peak frequency variation vs. the (a) UC thickness t and (b) edge size a. The error bars on the experimental results are calculated as the peak width.

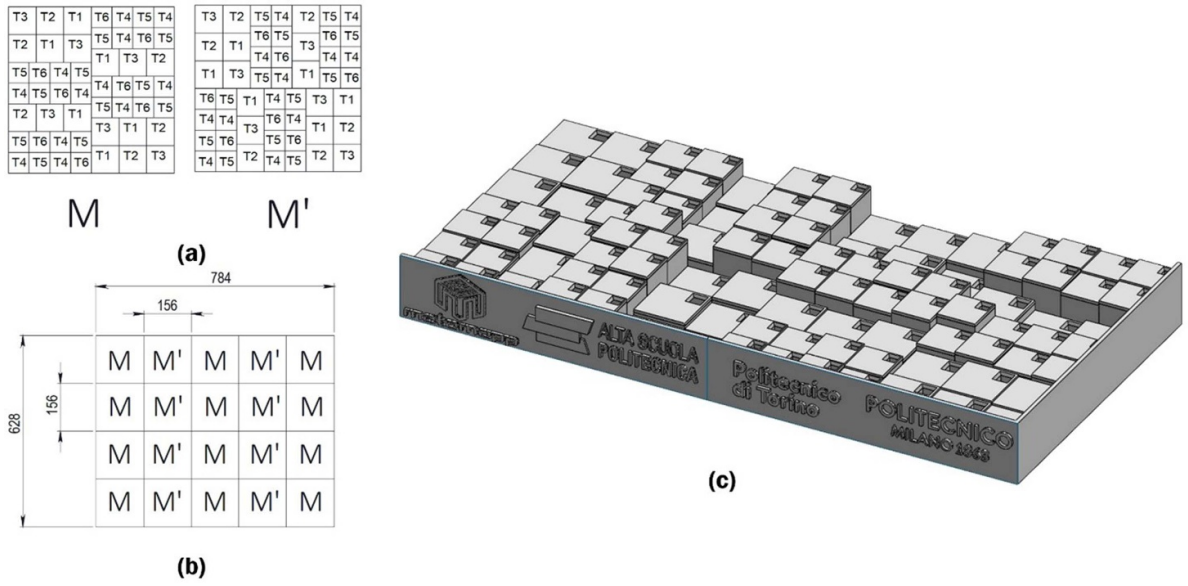


Figure 8. Modular elements of the complete sound absorption panel. (a) Two adjacent macro-cells. Each macro-cell consists of several UCs of edge size a_1 and a_2 with varying thicknesses (T1–T6); (b) Schematic top view of the final panel, consisting of a regular arrangement of M and M′ macrocells (geometrical sizes are indicated in mm); Adjacent macro-cells are reflected and rotated by 90° in order to guarantee a globally homogeneous spectral response. (c) 3D view of two adjacent macrocells.

4.3. AM panel characterization

The measurement of the sound absorption of the complete panel is performed in a small-scale reverberation room at the Politecnico di Torino. A full validation of the performance of the room is presented in [48], highlighting the 400–5000 Hz working frequency range. The mean reverberation time of the empty room between 100 Hz and 5000 Hz is of 0.95 s with a Schroeder frequency f_s of 1152 Hz [49]. In order to ensure a high diffusivity of the sound field, the room is equipped with 8 diffusers on the ceiling, covering 13.5% of the total room area. The panel characterization procedure consists in using the integrated impulse response method [43] for simultaneous measurements on six different microphone positions in two conditions, i.e. with and without the sample on the floor of the room. The measurement chain includes a set-up of six 1/4' BSWA Tech MPA451 microphones and ICP104 (BSWA Technology Co.,

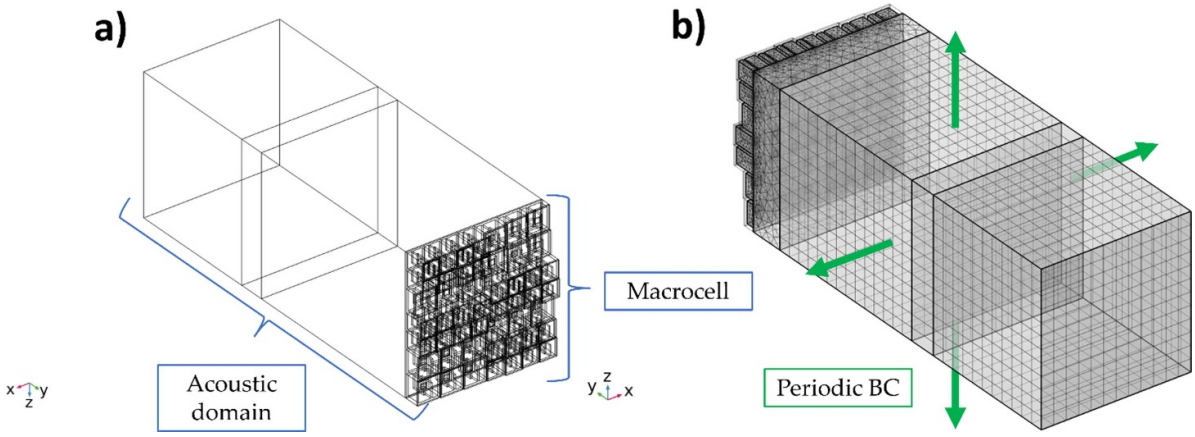


Figure 9. FE model of the AM panel: (a) rectangular duct ('acoustic domain') in which acoustic wave propagation is simulated, with normal incidence on the labyrinthine AM panel and backing cavity; (b) corresponding FE mesh, with refinement in the AM region.

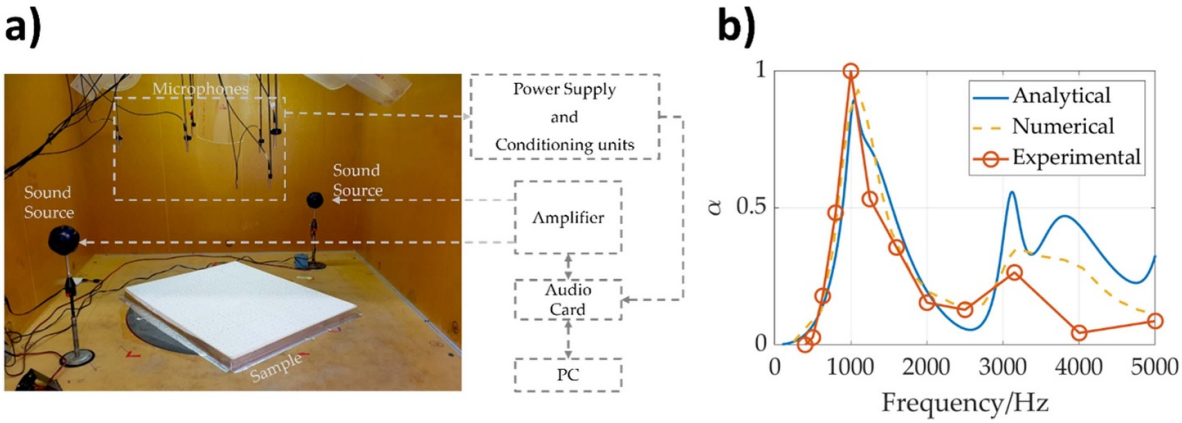


Figure 10. (a) AM panel absorption measurement setup in the small-scale reverberation room; (b) Absorption spectrum of the labyrinthine AM panel in the reverberation room measurements. The experimental spectrum is compared to the analytically and numerically predicted ones.

Ltd, Beijing, China), two ITA High-Frequency Dodecahedron Loudspeakers with their specific ITA power amplifiers (ITA-RWTH, Aachen, Germany) and a Roland OctaCapture UA-1010 sound card (Roland Corporation, Japan) in order to perform 12 measurements (the minimum number required by ISO 354 [43]). We use a Matlab code combined with the functions of the ITA-Toolbox (an open-source toolbox from RWTH-Aachen, Germany) for sound generation, recording and signal processing. We perform a spatial averaging considering all the 12 sources and microphone combinations, checking the temperature ($\geqslant$15 °C) and humidity (between 30–90%) conditions. According to the ISO 354 standard [50], the equivalent specimen absorption area is calculated (in square meters), using the formula:

$$A_T = 55.3V\left(\frac{1}{c_2 t_2} - \frac{1}{c_1 t_1}\right) - 4V(m_2 - m_1)\,, \qquad (2)$$

where t_1, t_2 are the reverberation times (in s) of the chamber without and with the specimen, respectively; V is the volume of the empty reverberation room in m^3; c_1 and c_2 are the sound propagation speeds in air in the reverberation room without and with the sample, respectively; m_1, m_2 are the power attenuation coefficients of the climatic conditions in the reverberation room without and with the sample. Finally, the random-incidence absorption coefficient of the tested specimen is computed as $\alpha = \frac{A_T}{S}$, where S is the area covered by the test specimen, expressed in m^2.

4.4. AM panel sound absorption results

As shown in figure 7, the panel has a flat upper surface and an uneven lower surface. The upper surface is equipped with apertures from which the sound waves access the UCs, while the lower surface is fully sealed. Figure 10(a) displays the experimental test configuration of the panel: the flat surface is facing the sound source. This configuration corresponds to the configuration in which the panel has an attenuating effect on sound waves. In figure 10(b), the comparison of analytically, numerically and experimentally predicted absorption spectra is shown. Frequencies of interest are reported in third-octave bands in the range of interest (250–5000 Hz). The orange line shows the effective sound absorption of the upper surface,

which is close to the ideal value of 1 in the desired frequency range between 800 and 1300 Hz. Additionally, an analytical absorption curve (in blue) is obtained for a fine band spectrum computing the overall impedance of the panel considering the UCs working in parallel, as detailed in [39]. Although the pressure field of the analytical and numerical model impinges normally on the surface, while in experimental testing conditions of the reverberation room there is a diffused field, the two absorption spectra show good agreement in the main absorption peak range, indicating the effectiveness of the panel also in non-normal conditions. Numerical results, calculated with the model described in the previous Section (again for normal incidence), are also included in the plot in figure 10(b), showing excellent agreement with analytical and experimental results. Some discrepancy emerges at higher frequencies (above 3 kHz) between experimental and predicted results, probably due to the greater influence of a non-normal incidence angle. Edge effects due to the finite sample size were not considered. As discussed in [48], these would become significant at frequencies below 400 Hz for the considered reverberation room and sample size. However, the impact of these effects is particularly significant at low frequencies in the case of thick samples and highly absorbing materials [51, 52].

5. Numerical evaluation of different labyrinthine sound absorption panel solutions

5.1. Macrocell with backing cavity

Given the promising results for the design procedure outlined in the previous Sections, and the good agreement between numerical and experimental results, a further numerical study is performed to evaluate possible developments of the AM-based sound absorption panel. The objective is to assess its acoustic performance under different design configurations. More specifically, three additional configurations are assessed: (a) the addition of a melamine foam inside the UCs of the panel; (b) the addition of a rigid rear backing cavity applied in correspondence with the uneven bottom surface of the panel (in this case with open apertures), with/without melamine foam filling; (c) a combination of (a) + (b). The acoustic performance of each of these features can be studied and compared to the original configuration (taken as a baseline), again performing FE simulations with COMSOL Multiphysics, focusing on a single marcocell, taken as representative of the panel behavior. Again, thermo-viscous effects need to be accounted for.

In the second configuration, the AM panel is coupled to an additional acoustic domain of a depth equal to four times its side length (figures 11(a) and (b)). Non-reflective perfectly matched layer boundary conditions are applied to the back of the acoustic domain. Once again, structural domains are considered perfectly rigid, since results from fully vibro-acoustic and simple acoustic simulations give rise to negligible differences. The foam material is chosen as melanine, whose properties are summarized in table 1.

Table 1. Melamine foam material properties used in FE simulations.

Parameter	Value
Porosity	0.995
Flow resistivity	10 500 Pa·s m^{-2}
Thermal characteristic length	470 μm
Viscous characteristic length	240 μm
Tortuosity factor	1.0059

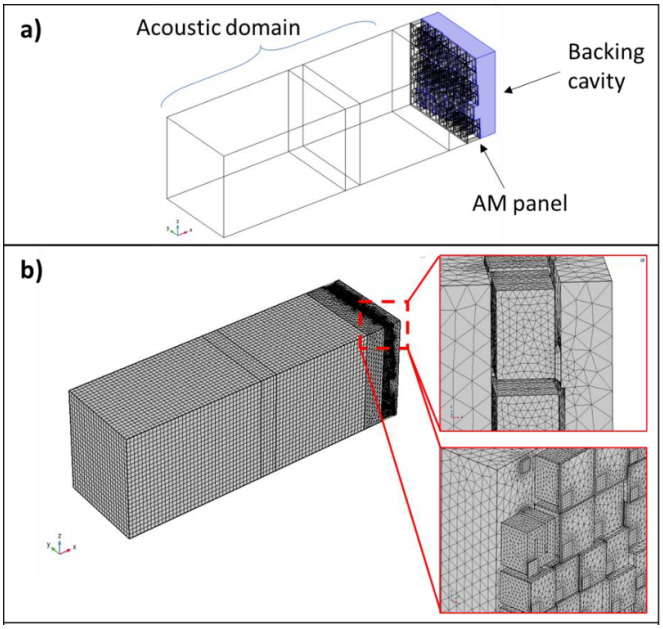


Figure 11. FE model of the AM panel with a backing cavity. (a) Rectangular duct ('acoustic domain') in which acoustic wave propagation is simulated, with normal incidence on the labyrinthine AM panel and backing cavity. (b) Corresponding FE mesh, with refinement in the AM region, as shown in the side and rear view enlargements.

5.2. Results

Figure 12 shows the calculated absorption coefficient in the three considered cases. The baseline simulation, corresponding to the dashed curve in figure 10(b), is shown in red. The effect of the presence of a backing cavity (5 mm thick) filled with melamine foam (green dashed curve in figure 12) is to shift absorption peaks to lower frequencies (the lowest from 1 kHz to about 700 Hz), with a beneficial effect for the attenuation of low frequencies. The addition of a foam filling in the AM cavities, on the other hand, leads to a more uniform absorption coefficient over the whole frequency range, at the expense of a lower efficiency at the AM working frequencies. This solution can however be useful in the case where a more distributed attenuation effect is required over the whole frequency range, rather than at specific target frequencies. Other types of foams can also be considered to optimize the combined effect with the AM.

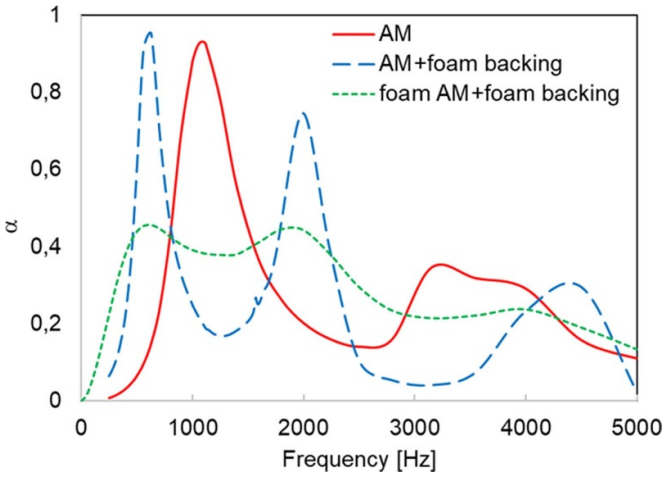


Figure 12. FE simulation results for absorption coefficient vs. frequency for different sound attenuating panel solutions: the initial panel (AM), with the addition of a 5 mm foam-filled backing on the panel (AM + foam backing) and additionally filling the AM cavities with foam (foam AM +foam backing).

6. Conclusions

In this work, we have provided an experimental proof of concept for a novel approach to noise attenuation, exploiting a rainbow-based design using labyrinthine metamaterials and combining UCs of varying thickness and lateral size in a quasi-periodic arrangement that ensures good homogeneity in the panel response. We have described the full design and validation procedure, from numerical design and modeling of the UC, to its characterization in an impedance tube, to the design of the macrocells composing the panel, and its realization using SLS. The final structure has then been characterized experimentally in a small-scale reverberation chamber, demonstrating a close to ideal absorption over the targeted low frequency range, centered at 1 kHz, thus validating the approach. Finally, detailed FE simulations have allowed to evaluate possible improvements/modifications to the panel by adding a foam filling and a foam backing cavity. The proposed prototype can be further developed, and thanks to its modular design, can be employed in diverse applications, e.g. in room acoustics, in automotive parts, or aeronautics in general. This approach, together with other metamaterial-based solutions proposed in the literature, contributes to an alternative (or complementary) route to the use of traditional sound absorbing materials in noise control. The proposed solution can be particularly attractive due to the reduced thickness of the panels and relatively small density of the required parts emerging from the subwavelength nature of the labyrinthine metamaterials used in the design.

Data availability statement

The data that support the findings of this study are available upon reasonable request from the authors.

Acknowledgments

F N, V H K, L B, E M, D P, M Z, A S G, L S, F B thank the Alta Scuola Politecnica project 'MetaMAPP'. F N, A S G, N P, L Sa and F B are supported by the H2020 FET Open 'Boheme' Grant No. 863179.

Appendix

The general theory of sound propagation in a cylindric tube in presence of viscous-thermal losses was initially developed by Kirchhoff [53] using the linearized Navier–Stokes equation. Given the complexity of the analytical solution, Zwikker and Kosten [54] developed approximate solutions for narrow and wide tube diameters. Subsequently, Stinson [42] derived an approximate solution for an infinitely long tube with arbitrary cross-sectional shape. This model was employed to calculate the variation of impedance along the coiled-up tube (figure 1(b)). The thin inlet was instead described using the JCA model, as pointed out in [55]. The model allows to include not only the losses taking place along the inlet, but also those around the aperture due to the sudden cross-section variation.

Considering the rigid backing as a wall of infinite impedance we can write the impedance beneath the aperture ($Z\left(x_1^-\right)$) as:

$$Z\left(x_1^-\right) = -iZ^{\,\mathrm{c}}_{\,\mathrm{eff}}\cot\left(k^c_{\mathrm{eff}}x_1\right), \tag{3}$$

where $x_1 = 3l_c$, $l_c = \sqrt{a^2+w^2} - \psi$, and x_1^- indicates the x_1 value inside the cavity. ψ is an empirical correction factor that models the effective propagation path due to the initial assumptions of an infinite straight tube of the Stinson's model [30]. The comparison with experimental results have shown that this factor is approximately 9% or less of the UC size a. $Z^c_{\mathrm{eff}} = \sqrt{\rho^c_{\mathrm{eff}}/C^c_{\mathrm{eff}}}$, and $k^c_{\mathrm{eff}} = \omega\sqrt{\rho^c_{\mathrm{eff}}C^c_{\mathrm{eff}}}$ are the effective impedance and propagation constants, where ω is the angular frequency, and ρ^c_{eff} and C^c_{eff} are the complex density and compressibility function averaged over the channel cross-section according to the Stinson's approximation:

$$\rho^c_{\mathrm{eff}} = \frac{\rho_0\nu w^2t^2}{4i\omega}\left[\sum_{k=1}^{\infty}\sum_{n=1}^{\infty}\left[\alpha_k^2\beta_n^2\left(\alpha_k^2+\beta_n^2+\frac{i\omega}{\nu}\right)\right]^{-1}\right]^{-1}, \tag{4}$$

$$C^c_{\mathrm{eff}} = \frac{1}{P_0}\left[1-\frac{4i\omega(\gamma-1)}{\nu' w^2t^2}\sum_{k=1}^{\infty}\sum_{n=1}^{\infty}\left[\alpha_k^2\beta_n^2\left(\alpha_k^2+\beta_n^2+\frac{i\omega\gamma}{\nu'}\right)\right]^{-1}\right], \tag{5}$$

where $\alpha_m = \frac{\left(m+\frac{1}{2}\right)\pi}{w/2}$, $\beta_m = \frac{\left(m+\frac{1}{2}\right)\pi}{t/2}$, $\nu = \eta/\rho_0$, η is the air dynamic viscosity, and $\nu' = \kappa/\rho_0 C_v$ with κ the thermal conductivity of air, C_v the specific heat at constant volume of air and $\gamma = C_p/C_v$ where C_p is the specific heat at constant pressure of air. The impedance at the aperture's top entrance ($Z\left(x_2^-\right)$) is computed as:

$$Z\left(x_2^-\right) = Z^{\,\mathrm{a}}_{\,\mathrm{eff}}\frac{-iZ\left(x_1^+\right)\cot\left(k^a_{\mathrm{eff}}x_2\right)+Z^{\,\mathrm{a}}_{\,\mathrm{eff}}}{Z\left(x_1^+\right)-iZ^{\,\mathrm{a}}_{\,\mathrm{eff}}\cot\left(k^a_{\mathrm{eff}}x_2\right)}, \tag{6}$$

where and x_1^+ indicates the x_1 value inside the aperture, x_2^- indicates the x_2 value inside the aperture, $Z\left(x_1^+\right) = Z\left(x_1^-\right)\frac{S_A}{S_C}$, with $S_A = w^2$ and $S_C = w \times t$, $Z^{\mathrm{a}}_{\mathrm{eff}} = \sqrt{\rho^a_{\mathrm{eff}}/C^a_{\mathrm{eff}}}$, $k^a_{\mathrm{eff}} = \omega\sqrt{\rho^a_{\mathrm{eff}} C^a_{\mathrm{eff}}}$ are the effective impedance and propagation constant for the aperture and where ρ^a_{eff} and C^a_{eff} are the complex density and compressibility functions at the aperture according to the JCA model [39]:

$$\rho^a_{\mathrm{eff}} = \frac{\alpha_\infty \rho_0}{\Phi} + \frac{\sigma}{i\omega}\sqrt{1 + \frac{4i\alpha_\infty^2 \eta \rho_0 \omega}{\sigma^2 \Lambda^2 \Phi^2}}, \tag{7}$$

$$C^a_{\mathrm{eff}} = \frac{\gamma - (\gamma - 1)\left[1 + \frac{8\eta}{i\rho_0\omega Pr\Lambda'^2}\sqrt{1 + \frac{i\rho_0\omega Pr\Lambda'^2}{16\eta}}\right]^{-1}}{\gamma P_0/\Phi}, \tag{8}$$

where $\alpha_\infty = 1$ is the tortuosity of the aperture, $\Phi = 1$ is the porosity of the panel (see table 1), Λ and Λ' are the viscous and thermal characteristic lengths, which in this case are both equal to the hydraulic radius of the aperture, here computed as $r_{\mathrm{hyd}} = w/4$. $\sigma = [(\frac{2h}{r_{\mathrm{hyd}}} + 1)(\alpha_s R_s/\Phi)(1/h)]S_A/S_T$, where α_s is an empirical fitting parameter accounting for the viscous effects occurring at sharp edges [39] and $R_s = \frac{1}{2}\sqrt{2\eta\omega\rho_0}$ is the specific airflow resistance.

Finally, the impedance at the surface is computed as:

$$Z_S = Z\left(x_2^+\right) = Z\left(x_2^-\right)\frac{S_T}{S_A}. \tag{9}$$

Where x_2^+ indicates the x_2 value inside the tube, and S_T is the cross section area of the Kundt's Tube (diameter $\varphi_0 =$ 35 mm) in which the relative sample is experimentally measured. The analytical absorption spectrum (figure 2(a)) obtained setting $\psi = 0$, and $\alpha_s = 1$, shows a perfect absorption peak attained at 1370 Hz, i.e. for a normal incident acoustic wave of wavelength $\lambda \sim 250$ mm, which is about 26 times larger than the UC thickness.

ORCID iDs

A S Gliozzi https://orcid.org/0000-0003-1084-0444
A O Krushynska https://orcid.org/0000-0003-3259-2592
N Pugno https://orcid.org/0000-0003-2136-2396
F Bosia https://orcid.org/0000-0002-2886-4519

References

[1] Ma G and Sheng P 2016 Acoustic metamaterials: from local resonances to broad horizons *Sci. Adv.* **2** e1501595
[2] Assouar B, Liang B, Wu Y, Li Y, Cheng J C and Jing Y 2018 Acoustic metasurfaces *Nat. Rev. Mater.* **3** 460–72
[3] Ge H, Yang M, Ma C, Lu M H, Chen Y F, Fang N and Sheng P 2018 Breaking the barriers: advances in acoustic functional materials *Natl Sci. Rev.* **5** 159–82
[4] Zhang X, Qu Z and Wang H 2020 Engineering acoustic metamaterials for sound absorption: from uniform to gradient structures *iScience* **23** 101110
[5] Kumar S and Lee H 2019 The present and future role of acoustic metamaterials for architectural and urban noise mitigations *Acoustics* **1** 590–607
[6] Li J, Wen X and Sheng P 2021 Acoustic metamaterials *J. Appl. Phys.* **129** 171103
[7] Langfeldt F and Gleine W 2019 Improved sound transmission loss of glass wool with acoustic metamaterials *Proc. 26th Int. Congress on Sound and Vibration* (*ICSV 2019*)
[8] Palma G, Mao H, Burghignoli L, Göransson P and Iemma U 2018 Acoustic metamaterials in aeronautics *Appl. Sci.* **8** 971
[9] Yang M and Sheng P 2017 Sound absorption structures: from porous media to acoustic metamaterials *Annu. Rev. Mater. Res.* **47** 83–114
[10] Dong C, Liu Z, Pierce R, Liu X and Yi X 2023 Sound absorption performance of a micro perforated sandwich panel with honeycomb-hierarchical pore structure core *Appl. Acoust.* **203** 109200
[11] Zhao L and Zhou S 2019 Compact acoustic rainbow trapping in a bioinspired spiral array of graded locally resonant metamaterials *Sensors* **19** 788
[12] Yang M, Ma G, Yang Z and Sheng P 2013 Coupled membranes with doubly negative mass density and bulk modulus *Phys. Rev. Lett.* **110** 134301
[13] Ma G, Yang M, Xiao S, Yang Z and Sheng P 2014 Acoustic metasurface with hybrid resonances *Nat. Mater.* **13** 873–8
[14] Romero-García V, Theocharis G, Richoux O and Pagneux V 2016 Use of complex frequency plane to design broadband and sub-wavelength absorbers *J. Acoust. Soc. Am.* **139** 3395–403
[15] Jiménez N, Huang W, Romero-García V, Pagneux V and Groby J P 2016 Ultra-thin metamaterial for perfect and quasi-omnidirectional sound absorption *Appl. Phys. Lett.* **109** 121902
[16] Romero-Garciá V, Theocharis G, Richoux O, Merkel A, Tournat V and Pagneux V 2016 Perfect and broadband acoustic absorption by critically coupled sub-wavelength resonators *Sci. Rep.* **6** 19519
[17] Jiménez N, Romero-García V, Pagneux V and Groby J-P 2017 Rainbow-trapping absorbers: broadband, perfect and asymmetric sound absorption by subwavelength panels for transmission problems *Sci. Rep.* **7** 13595
[18] Boulvert J, Costa-Baptista J, Cavalieri T, Romero-García V, Gabard G, Fotsing E R, Ross A, Perna M, Mardjono J and Groby J-P 2020 Folded metaporous material for sub-wavelength and broadband perfect sound absorption *Appl. Phys. Lett.* **117** 251902
[19] Ramos D, Godinho L, Amado-Mendes P and Mareze P 2022 Broadband low-frequency bidimensional honeycomb lattice metastructure based on the coupling of subwavelength resonators *Appl. Acoust.* **199** 109038
[20] Wang G, Luo G, Xiang L and Yin X 2023 Low-frequency broadband absorber with coherent coupling based on perforated panel and space-coiling channels *J. Appl. Phys.* **56** 495102
[21] Boulvert J, Humbert T, Romero-García V, Gabard G, Fotsing E R, Ross A, Mardjono J and Groby J-P 2022 Perfect, broadband, and sub-wavelength absorption with asymmetric absorbers: realization for duct acoustics with 3D printed porous resonators *J. Sound Vib.* **523** 116687
[22] Liang Z and Li J 2012 Extreme acoustic metamaterial by coiling up space *Phys. Rev. Lett.* **108** 114301
[23] Liang Z, Feng T, Lok S, Liu F, Ng K B, Chan C H, Wang J, Han S, Lee S and Li J 2013 Space-coiling metamaterials with double negativity and conical dispersion *Sci. Rep.* **3** 1614
[24] Man X, Luo Z, Liu J and Xia B 2019 Hilbert fractal acoustic metamaterials with negative mass density and bulk modulus on subwavelength scale *Mater. Des.* **180** 107911

[25] Xie Y, Konneker A, Popa B I and Cummer S A 2013 Tapered labyrinthine acoustic metamaterials for broadband impedance matching *Appl. Phys. Lett.* **103** 201906
[26] Maurya S K, Pandey A, Shukla S and Saxena S 2016 Double negativity in 3D space coiling metamaterials *Sci. Rep.* **6** 33683
[27] Liu Y, Xu W, Chen M, Yang T, Wang K, Huang X, Jiang H and Wang Y 2020 Three-dimensional fractal structure with double negative and density-near-zero properties on a subwavelength scale *Mater. Des.* **188** 108470
[28] Song G Y, Cheng Q, Huang B, Dong H Y and Cui T J 2016 Broadband fractal acoustic metamaterials for low-frequency sound attenuation *Appl. Phys. Lett.* **109** 131901
[29] Zhang C and Hu X 2016 Three-dimensional single-port labyrinthine acoustic metamaterial: perfect absorption with large bandwidth and tunability *Phys. Rev. Appl.* **6** 064025
[30] Krushynska A O, Bosia F, Miniaci M and Pugno N M 2017 Spider web-structured labyrinthine acoustic metamaterials for low-frequency sound control *New J. Phys.* **19** 105001
[31] Krushynska A O, Bosia F and Pugno N M 2017 Labyrinthine acoustic metamaterials with space-coiling channels for low-frequency sound control (arXiv:1712.06063)
[32] Molerón M, Serra-Garcia M and Daraio C 2016 Visco-thermal effects in acoustic metamaterials: from total transmission to total reflection and high absorption *New J. Phys.* **18** 033003
[33] Palma G, Burghignoli L, Centracchio F and Iemma U 2021 Innovative acoustic treatments of nacelle intakes based on optimised metamaterials *Aerospace* **8** 296
[34] Ghinet S, Bouche P, Padois T, Pires L, Doutres O, Kone T C, Triki K, Abdelkader F, Panneton R and Atalla N 2020 Experimental validation of acoustic metamaterials noise attenuation performance for aircraft cabin applications *Proc. 2020 Int. Congress on Noise Control Engineering* (*INTER-NOISE 2020*)
[35] Cox T and d'Antonio P 2016 *Acoustic Absorbers and Diffusers: Theory, Design and Application* (CRC Press)
[36] Jiménez N, Umnova O and Groby J-P 2021 *Acoustic Waves in Periodic Structures, Metamaterials, and Porous Media Ch. The Transfer Matrix Method in Acoustics* (Springer) pp 103–64
[37] Laude V 2020 *Phononic Crystals* (de Gruyter)
[38] Krushynska A O, Bosia F and Pugno N M 2018 Labyrinthine acoustic metamaterials with space-coiling channels for low-frequency sound control *Acta Acust. United Acust.* **104** 200–10
[39] Magnani A, Marescotti C and Pompoli F 2022 Acoustic absorption modeling of single and multiple coiled-up resonators *Appl. Acoust.* **186** 108504
[40] Wang Y, Zhao H, Yang H, Zhong J, Zhao D, Lu Z and Wen J 2018 A tunable sound-absorbing metamaterial based on coiled-up space *J. Appl. Phys.* **123** 185109
[41] Almeida G N, Vergara E F, Barbosa L R and Brum R 2021 Low-frequency sound absorption of a metamaterial with symmetrical-coiled-up spaces *Appl. Acoust.* **172** 107593
[42] Stinson M R 1991 The propagation of plane sound waves in narrow and wide circular tubes, and generalization to uniform tubes of arbitrary cross-sectional shape *J. Acoust. Soc. Am.* **89** 550–8
[43] ISO 354 2003 *Acoustics—measurement of sound absorption in a reverberation room* 3 (International Standard)
[44] ASTM 1990 Standard test method for impedance and absorption of acoustical materials using a tube, two microphones and a digital frequency analysis system *American Society for Testing of Materials*
[45] ASTM E2611 2019 Standard test method for normal incidence determination of porous material acoustical properties based on the transfer matrix method E2611 *American Society for Testing of Materials*
[46] Kuttruff H 2007 *Acoustics: An Introduction* (CRC Press)
[47] Pilon D, Panneton R and Sgard F 2004 Behavioral criterion quantifying the effects of circumferential air gaps on porous materials in the standing wave tube *J. Acoust. Soc. Am.* **116** 344–56
[48] Shtrepi L and Prato A 2020 Towards a sustainable approach for sound absorption assessment of building materials: validation of small-scale reverberation room measurements *Appl. Acoust.* **165** 107304
[49] Schroeder M R 1996 The 'Schroeder frequency' revisited *J. Acoust. Soc. Am.* **99** 3240–1
[50] Vercammen M 2010 Improving the accuracy of sound absorption measurement according to ISO 354 *Proc. Int. Symp. on Room Acoustics* (*Melbourne, Australia*) pp 29–31
[51] De Bruijn A 2008 On the scattering of a plane wave by porous sound-absorbing strip *J. Acoust. Soc. Am.* **123** 3141
[52] Duval A, Rondeau J-F, Dejeager L, Sgard F and Atalla N 2010 Diffuse field absorption coefficient simulation of porous materials in small reverberant rooms: finite size and diffusivity issues *10ème Congrès Français d'Acoustique*
[53] Kirchhoff G 1868 Ueber den Einfluss der Wärmeleitung in einem Gase auf die Schallbewegung *Ann. Phys.* **210** 177–93
[54] Zwikker C and Kosten C W 1949 *Sound Absorbing Materials* (Elsevier)
[55] Atalla N and Sgard F 2007 Modeling of perforated plates and screens using rigid frame porous models *J. Sound Vib.* **303** 195–208